Detection of catalytic intermediates at an electrode surface during carbon dioxide reduction by an earth-abundant catalyst

Gaia Neri,[a] *James. J. Walsh*[a ‡], *Gilberto Teobaldi,*[a,b] *Paul M. Donaldson*[c*] *and Alexander J. Cowan*[a *]

[a]Department of Chemistry and Stephenson Institute for Renewable Energy, University of Liverpool, L69 7ZD, Liverpool, UK, acowan@liverpool.ac.uk,

[b]Beijing Computational Science Research Center 100193 Beijing, China

[c]Central Laser Facility, STFC Rutherford Appleton Laboratory, Harwell, Didcot, Oxfordshire, OX11 0QX, UK, paul.donaldson@stfc.ac.uk

[‡]Current address, School of Chemical Sciences and National Centre for Sensor Research, Dublin City University, Glasnevin, Dublin 9, Ireland

Abstract:

Electrocatalytic reduction of CO_2 offers a sustainable route to the many carbon fuels and feedstocks which society relies upon. [*fac*-Mn(bpy)$(CO)_3$Br] (bpy = 2,2-bipyridine) is one of the most promising and intensely studied CO_2 reduction electrocatalysts. However, the catalytic mechanism remains experimentally unproven and many key intermediates of the prototypical catalyst have not been observed. Here we report the use of vibrational sum-frequency generation (VSFG) spectroscopy to study the catalytic intermediates during CO_2 reduction in-situ at the electrode surface. We explore the complex, applied-potential and acid-dependent, mechanistic pathways and provide evidence of the theoretically derived mechanisms. Demonstrating the ability to detect the key species that are only transiently present at the electrode surface is important as the need for improved mechanistic understanding is a common theme throughout the field of molecular electrocatalysis.

Article:

Improved molecular electrocatalysts will be key in unlocking the potential of new clean energy technologies. Intense efforts are being expended world-wide to develop electrocatalysts for a range of reactions including: O_2 reduction, CO_2 reduction and H_2 evolution with potential impacts across sustainable fuel generation, utilisation and electrochemical energy storage.[1–3] Therefore it is important to identify new tools that can provide the mechanistic insights required to enable these catalyst development programmes.

A critical problem is that many spectroelectrochemical (SEC) experiments require the build-up of a sufficient concentration of the electrochemically generated species in the bulk solution to enable detection.[4] In reality intermediates during molecular electrocatalysis may only be present transiently at the electrode surface or within the electric double layer (EDL). Therefore, whilst the identification of short-lived electrochemical intermediates at interfaces is challenging it remains an important goal. VSFG spectroscopy is an inherently interface specific spectroscopy.[5] The theory behind VSFG is reviewed in detail elsewhere.[6,7] Briefly, during a broad-band VSFG experiment short (fs) IR and (ps) visible laser pulses are overlapped in time and space at the interface of interest and light generated at the sum of the frequency of the IR and visible pulses is detected. Due to interference effects typically

only light from interfacial regions is detected as light from the bulk is totally extinguished. A large resonant enhancement in the sum frequency light is measured when the IR frequency matches an interfacial vibrational mode.

The inherent interfacial selectivity of VSFG spectroscopy has been exploited to study a wide range of electrolyte/electrode interfaces providing important information on the packing and structure of the EDL and on catalytic processes during heterogeneous electrocatalysis.[8–11] In contrast, despite intense interest in the field, homogenous electrocatalysis remains largely unexplored by VSFG spectroscopy. Although VSFG has provided important details on the binding modes[12,13] and vibrational relaxation kinetics[14,15] of surface immobilised complexes the majority of studies have been carried out in the absence of an applied potential. Indeed prior to the work reported here we are only aware of one previous VSFG study of a molecular electrocatalyst under potentiostatic control, where we[16] examined the behaviour of [Mo(bpy)(CO)$_4$] at Au and Pt electrodes. We were able to offer insight into the work of Tory et al., who first demonstrated the critical role of the Au surface for these catalysts,[17] however we were unable to identify any catalytic intermediates formed following reduction of the catalyst precursor. Nonetheless, this study did indicate that sufficient ordering occurs within the EDL at certain applied potentials, enabling measurements of the complexes' VSFG spectrum at the electrode.

Since its initial report in 2011, [*fac*-Mn(bpy)(CO)$_3$X]^n (X = Br$^-$ or solvent (**1**), n = 0 or +1, figure 1), has become one of the most widely studied electrocatalysts for the reduction of CO_2 to CO.[18] Despite advances in electrocatalytic activity[19–24] the full mechanism of CO_2 reduction for this class of catalysts remains experimentally un-proven. It is known[25] that reduction of two equivalents of **1** leads to formation of [(Mn(bpy)(CO)$_3$)$_2$] (**2**) at -1.12 V_{SCE} at room temperature. At potentials negative of -1.50 V_{SCE} **2** is reduced to [Mn(bpy)(CO)$_3$]$^-$ (**3**, figure 1),[18,25] which is proposed to be the primary active catalyst for CO_2 reduction. An alternative pathway where CO_2 directly interacts with **2** has also been reported when 4,4'-alkyl substituted bipyridine ligands are used.[26] At low temperatures[27] or when bulky[20] ligands are used **3** can also form following the reduction of [Mn(bpy)(CO)$_3$]$^\cdot$ at the first cathodic wave of the parent complex by an ECE mechanism. In the absence of CO_2 **3** reacts with proton sources to form [Mn(bpy)(CO)$_3$H] (**4**), with H_2 then formed.[28] In the presence of both CO_2 and a Brønsted acid CO evolution occurs with excellent selectivity and minimal H_2 production. Intriguingly without the acid, CO_2 reduction does not occur[29] in contrast to analogous rhenium complexes.[30] State-of-the-art DFT simulations have explored the critical role of the acid and identified a protonation assisted binding mechanism of CO_2 and the catalytic pathways upon which Figure 1 is based.[31–33] CO_2 binding to **3** and formation of [Mn(bpy)(CO)$_3$(CO$_2$)]$^-$ (**5**) is calculated to be endergonic in the absence of a suitable acid. However rapid protonation of **5** to form the more stable product [Mn(bpy)(CO)$_3$(CO$_2$H)] (**6**) can occur.[32,33] Once formed, **6** is thought to be able to react *via* two pathways.[31] The reduction first pathway to form [Mn(bpy)(CO)$_3$(CO$_2$H)]$^-$ (**7**) which is followed by protonation and water expulsion to yield [Mn(bpy)(CO)$_4$] (**9**). The reduction of **9** then leads to CO loss, regeneration of **3** and completion of the catalytic cycle. Alternatively **6** can be protonated (protonation first pathway) to yield [Mn(bpy)(CO)$_4$]$^+$ (**8**) which can then be reduced to form **9** prior to CO evolution.

The reduction potential for **6** (calculated -1.7 V_{SCE}) coupled to the calculated activation barrier for its protonation of between 12-22 kcal mol^{-1} depending on the acid source, has led to the prediction that the mechanism and turnover frequency (TOF) of catalysis by **1** is both potential and acid dependent.[32,33] In strong acids the "protonation first" pathway is predicted to occur at lower overpotentials whilst negative of -1.7 V_{SCE} the reduction first pathway dominates.[31] Solution based microkinetic simulations[32] have shown a good correlation between the observed catalytic TOF's and applied potential. However the key catalytic intermediates (**6**-**10**) and the proposed potential dependent switch in mechanism have not been experimentally observed with the prototypical complex **1**.[19,28,34]

Here we report a VSFG study of the very active CO_2 reduction **1**under potentiostatic control. Our *in-situ* VSFG study provides experimental observation of the proposed switch in pathway with **1**.

Critically, the observation of key intermediates not seen by bulk SEC methods demonstrates the wider value of VSFG for the study of complex molecular electrocatalytic mechanisms.

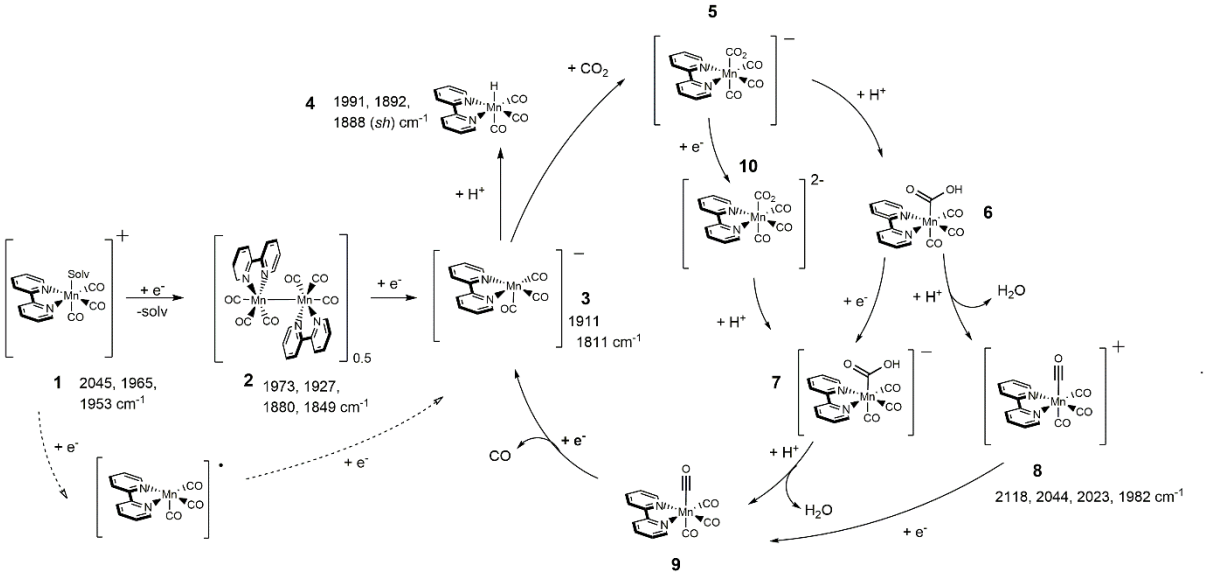

Figure 1. **Proposed electrocatalytic pathways for the reduction of CO_2 by 1.** *The scheme shows the proposed protonation first (**6-8-9**) and reduction first (**6-7-9**) mechanisms of CO_2 reduction by $[Mn(bpy)(CO)_3(solv)]^+$ (**1**) (solv = CH_3CN or when present H_2O) in the presence of a Brønsted acid. The Brønsted acid strength and applied potential are thought to control the relative contributions from each pathway. The catalytic cycle is based on theoretical calculations reported elsewhere.*[31–33] *ν(CO) IR wavenumbers are for solution species that have either been synthesised and found to be stable (**1**[22] and **8**[35]) or have been observed in past SEC studies (**2**[34], **3**[28] and **4**[28]). The dashed lines indicate an alternative pathway for the formation of **3** that has been determined to occur at low temperatures and also when bpy derivatives with bulky substituents are employed.*[2027]

Results

Cyclic voltammetry of 1 within the SEC cell. Cyclic voltammograms (CV's) of **1** in CH_3CN recorded within the SEC cell using an Au-Hg amalgam working electrode are shown in figure 2. Au-Hg provides both reflectivity in the visible region, a requirement for our VSFG experiment, and a suitable electrochemical window for use in the presence of organic acids such as trifluoroethanol (TFE). On Au-Hg **1** behaves similarly to previous reports using glassy carbon electrodes, with reductions of **1** and **2** occurring at -0.92 and -1.27 V_{Ag} respectively, corresponding to approximately -1.12 V_{SCE} and -1.47 V_{SCE}.[18] In-line with past studies an increased current density due to catalytic CO_2 reduction only occurs when both CO_2 and an acid source are present.[19] The similarity of the reduction potentials[18] to those previously reported coupled to the same catalytic behaviour suggests a common CO_2 reduction mechanism for both glassy carbon and Au-Hg electrodes.

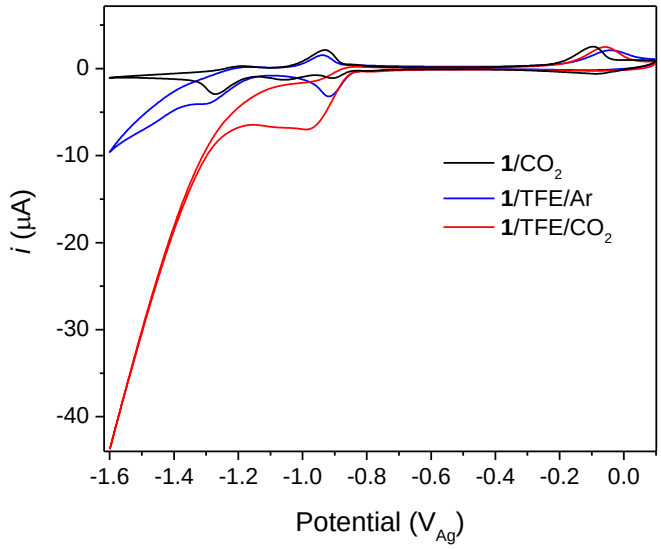

Figure 2: **CV's of 1 under argon and CO_2 in the presence or absence of TFE.** *In the presence of both an acid source (TFE) and CO_2, electrocatalytic CO_2 reduction occurs as indicated by the sharp increase in current (i). CV's are recorded within the SEC cell at 50 mVs^{-1} in CH_3CN and 0.1 M $TBAPF_6$ under the conditions indicated, TFE when present is at 1.5 M. Potentials are reported versus the Ag/Ag^+ pseudo reference electrode used in the SEC cell unless otherwise stated. The deviation from the peak shapes typically observed for freely diffusing species is due to the short distance between the electrode surface and the cell front window (50 μm), supplementary figure 1.*

In-situ VSFG spectra in the absence of CO_2 The VSFG spectra of **1** recorded during two successive CV measurements (10 mV s^{-1}) in acetonitrile with TFE (1.5 M) under argon are shown in figure 3. Under these conditions the current increase negative of -1.3 V_{Ag} is assigned to H_2 evolution. To enable the identification of resonant VSFG bands the non-resonant response of the Au-Hg/electrolyte interface was suppressed by the introduction of a 0.9 ps delay between the fs broad-band IR pulse and a time asymmetric picosecond (ps) visible (800 nm) laser pulse.[36] At open circuit we see no clear VSFG signals but as soon as a potential of 0.1 V_{Ag} is applied a ν(CO) mode at 2043 cm^{-1} appears, in addition to broad weak VSFG signals at *ca.* 1950 cm^{-1} (supplementary figure 2). These bands are readily assignable to $[Mn(bpy)(CO)_3(CH_3CN)]^+$ (**1**) through comparison to the FTIR of the starting solution, figures 3(c), supplementary table 1 and figures 2-4. As the potential of the electrode is made more negative we see an increase in the intensity of the VSFG bands of **1** indicating either an accumulation, or increased ordering, of this complex within the EDL and this point is further discussed in the Supplementary methods page 2. As the potential of the electrode is varied between 0.10 and -0.75 V_{Ag} we observe a shift of the ν(CO) band of **1** of *ca.* 35 cm V^{-1}. The potential dependence of vibrational modes is commonly interpreted to be due to Stark shifting effects occurring when a large electric field is present.[37] However it has also been recently highlighted that apparent potential dependent changes in the second-order spectral line-shapes can occur due to the changing contributions of dispersive and adsorptive third order components that arise within the EDL.[38] Both interpretations require **1** to experience a large electric field, confirming that during the VSFG experiment we are probing the vibrational spectra of **1** either at the electrode surface or within the EDL and that the spectral features are not due to "phantom transitions" arising from absorptive losses in the IR from the bulk solution.[8]

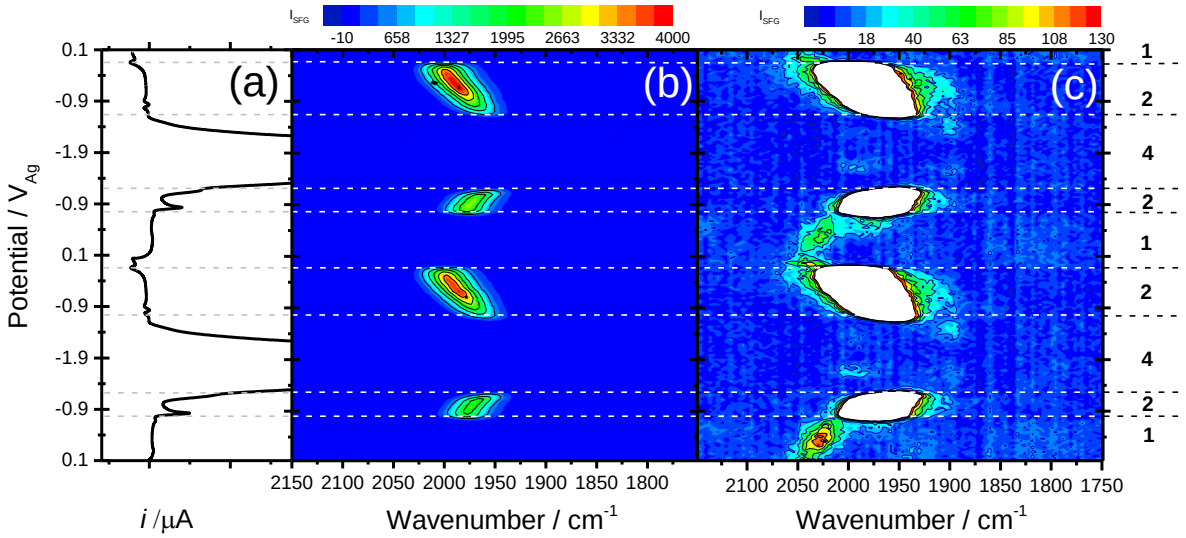

Figure 3: **VSFG spectra of 1 recorded during 2 successive CVs under Ar.** ***(a)*** *Current-voltage response recorded during the experiment at a scan rate of 10 mVs^{-1} (1 mM solution of* ***1*** *in CH_3CN (0.1 M $TBAPF_6$) and 1.5 M TFE under Ar).* ***(b)*** *VSFG contour plot, recorded with the IR laser centred at 1900 cm^{-1}, ppp polarization, which is dominated by* ***2*** *as described in the text.* ***(c)*** *Replotting the VSFG data over a more limited SFG intensity range (I_{SFG}) shows the interconversion of species* ***1-4*** *in figure 1. The formation of new VSFG bands occurs at potentials where we measure sharp changes in current (i) from our working electrode demonstrating that we are following the electrochemical processes occurring.*

At potentials negative of -0.75 V_{Ag} the ν(CO) band of **1** starts to decrease in intensity and a new intense band at 1974 cm^{-1} (-0.76 V_{Ag}) is formed, figure 3(b,c). This VSFG band matches a known ν(CO) band of $[(Mn(bpy)(CO)_3)_2]$, **2**, and the VSFG mode shifts to 1959 cm^{-1} at -1.25 V_{Ag}. The very strong VSFG response can be readily explained by the overlap of the UV/Vis absorption spectrum of **2** (λ_{max} 394, 461, 633, 806 nm)[18] with the 800 nm visible laser, giving rise to an additional electronic resonance enhancement. Under argon, following the reduction of **2** (<-1.3 V_{Ag}) we find weak VSFG bands at 1994 and 1898 cm^{-1} at *ca.* -1.5 V_{Ag} on the outward sweep and *ca.* -1.6 V_{Ag} on the return sweep of the CV, figure 3c. Careful inspection of these spectra (supplementary figure 5) shows that both modes are present at both potentials although with different relative intensities, suggesting that they are from a common intermediate undergoing an orientation change at the electrode. As we observe these bands at potentials close to where catalytic proton reduction occurs we assign them to the hydride intermediate **4** and we note good agreement to similar Mn-H intermediates reported elsewhere, supplementary table 1.[24,28] The observation of **4** but not **3** indicates that the formation of the hydride intermediate (**4**) is facile and rapid, making the selectivity of this catalyst towards CO_2 in the presence of high concentrations of acid remarkable.[19]

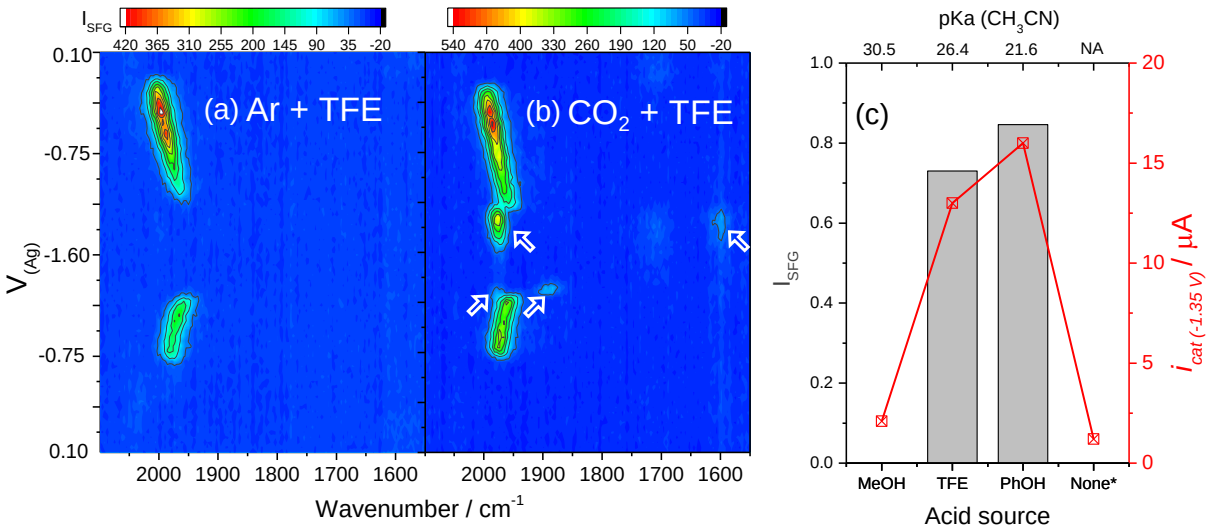

Figure 4: **VSFG spectra under CO_2 and TFE showing new bands assigned to catalytic intermediates.** ***(a)*** *VSFG spectra recorded during CV's (10 mV s^{-1}) of* ***1*** *(1 mM) in CH_3CN (0.1 M $TBAPF_6$) and 1.5 M TFE under Ar and* ***(b)*** *under CO_2. Under CO_2 new VSFG bands (highlighted with white arrows) are assigned to catalytic intermediate(s) during CO_2 reduction.* ***(c)*** *Shows the maximum intensity of the SFG band (I_{SFG}) of the CO_2 reduction intermediate (1976 cm^{-1}) with different acid sources. There is a direct correlation between the current (i) during CO_2 reduction at -1.35 V_{Ag} during the VSFG experiment (see supplementary figure 6 for CV's) and the intensity of the new VSFG band. pKa values are from reference [*[39]*] and to enable direct comparison of different VSFG experiments where alignment may be slightly different the I_{SFG} at 1976 cm^{-1} is normalised with respect to the measured intensity of the SFG mode of* ***2*** *at -0.2 V_{Ag}.*

In-situ evidence for the protonation first pathway under CO_2. VSFG spectra of **1** under CO_2 in CH_3CN and TFE show no evidence for the formation of **4** at 1994 and 1898 cm^{-1} at any applied potential, figure 4, supplementary figure 7. Instead, under CO_2 multiple new strong VSFG bands at 1976, 1600 cm^{-1} and 1875 cm^{-1} were observed in the potential region where catalytic reduction of CO_2 to CO occurs (-1.1 to -1.6 V_{Ag}), figure 4(b). Experiments in the absence of a deliberately added acid showed minimal current enhancement under CO_2 in-line with past studies[18] and the new VSFG bands were not observed, supplementary figure 8. VSFG experiments over the same potential window in the presence of TFE and CO_2 without the catalyst (**1**) also showed no clear VSFG signals. Therefore we assign the indicated VSFG bands at 1976, 1875 and 1600 cm^{-1} in figure 4(b) to CO_2 reduction intermediates, likely one (or more) of complexes **6-9**, figure 1. As hydride (**4**) formation was readily detectable in the same system under Ar it is clear that interaction of CO_2 with **3** must also be rapid. Furthermore the binding constant ($K_{CO2/H+}$) for **3** and CO_2 in the presence of an acid (here TFE) must strongly favour interaction with CO_2,[28] in-line with past observations on related Mn complexes with bulky ligands.[40] The observation of the effective suppression of hydride formation by CO_2 through competitive consumption of **3** provides a rationale for the excellent selectivity towards CO production.[19]

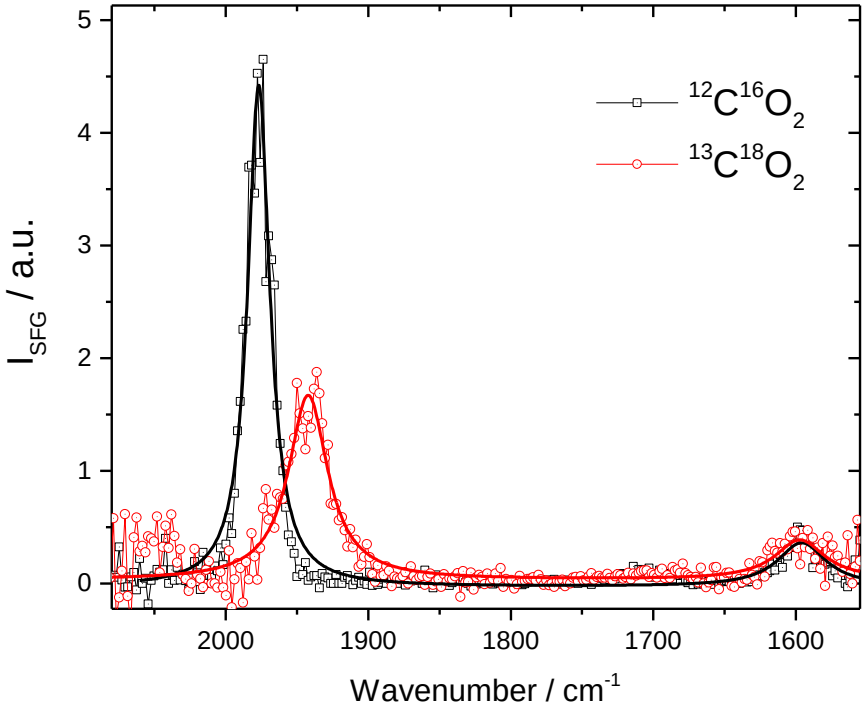

Figure 5: **VSFG spectra of the CO_2 reduction intermediate recorded using labelled CO_2** *When using $^{13}C^{18}O_2$ the band in the ν(CO) region is isotopically shifted. Spectra recorded at -1.25 V_{Ag} in CH_3CN (0.1 M $TBAPF_6$) and 1.5 M TFE under $^{12}C^{16}O_2$ (black) and $^{13}C^{18}O_2$ (red). Solid lines are the result of a multi-Lorentzian fit.*

We now turn to the assignment of the new VSFG bands present during catalytic CO_2 reduction in the presence of TFE at *ca.* 1976, 1875 and 1600 cm^{-1}, figure 4(b). The strongest new VSFG band (*ca.* 1976 cm^{-1}) is present on the return potential sweep between -1.40 V to -1.05 V_{Ag} with the highest intensity being between -1.20 and -1.10 V_{Ag}. The same feature is also briefly present at a lower intensity on the outward sweep between -1.20 and -1.35 V_{Ag}, peaking at -1.25 V_{Ag}, Figure 4(b). Concomitant with the formation of the band at 1976 cm^{-1}, shown below to be a ν(CO) mode of a metal carbonyl complex, we observe the formation of a band at 1600 cm^{-1}, figure 4b, supplementary figure 9. This spectral region is where both bipyridine ring modes and ν(OCO) modes occur. Theory predicts that either $[Mn(bpy)(CO)_3]^-$ (**3**)[32] or $[Mn(bpy)(CO)_3(CO_2H)]$ (**6**)[33] will accumulate at moderate applied potentials (when the protonation first pathway dominates), whilst either **6** or **7** may be present when the reduction first pathway dominates.[32,33] The ν(CO) band at 1976 cm^{-1} can't be assigned to **3** on the basis of the known spectrum of this complex, supplementary table 1. Experiments with isotopically labelled $^{13}C^{18}O_2$ also show no shift of the 1600 cm^{-1} VSFG band, figure 5. This alone does not immediately rule-out assignment to **6** or **7**. Indeed past studies on Mn carbonyl complexes with bulky ligands have reported the build-up of a complex assigned to a Mn(I) complex, potentially a Mn(I)-COOH intermediate analogous to **6**, on the basis of the ν(CO) modes without observation of the ν(OCO) mode which would have been anticipated to be present.[20,40] It does however suggest that the 1600 cm^{-1} band arises from the bipyridine ligand of the intermediate and not from a ν(OCO) mode, a full discussion of this assignment accompanies supplementary figures 9, 10.

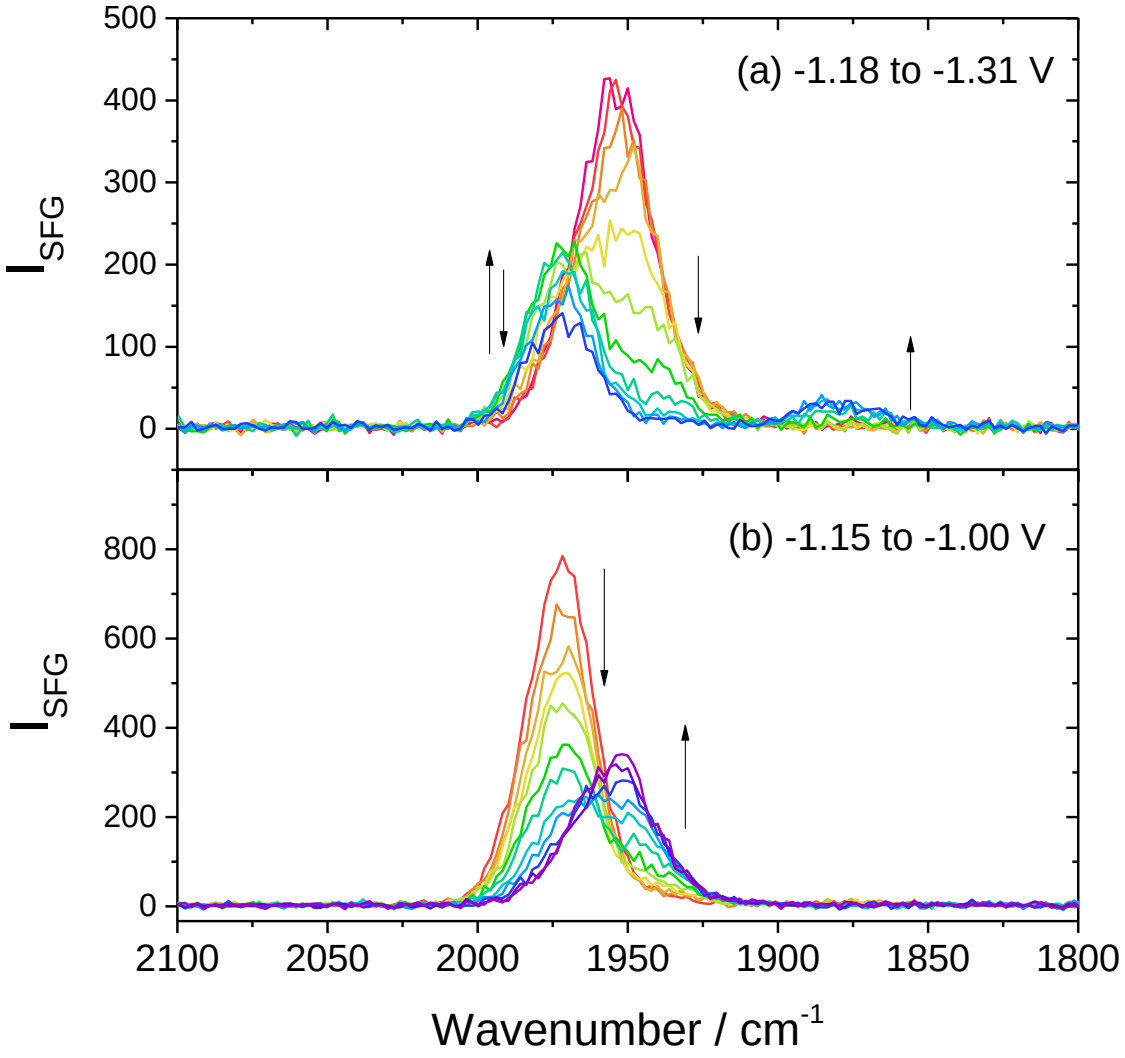

Figure 6: **VSFG spectra showing the potential dependence of the new CO_2 reduction intermediate ν(CO) mode**. *Spectra recorded during CV's of **1** (1 mM) in CH_3CN (0.1 M $TBAPF_6$) and 1.5 M TFE under CO_2 with the IR laser centred at 1900 cm^{-1}. **(a)** During the outward CV sweep the ν(CO) band assigned to **2** (ca. 1962 cm^{-1}) initially decreases as the new band at 1976 cm^{-1} grows in. As the potential is swept more negative the 1976 cm^{-1} band decrease as the 1875 cm^{-1} feature grows in. **(b)** On the return CV sweep the bands of the intermediate at 1976 cm^{-1} decreases in intensity as **2** is reformed.*

Interestingly a shift in the ν(CO) mode is observed from 1976 cm^{-1} ($^{12}C^{16}O_2$) to 1942 cm^{-1} ($^{13}C^{18}O_2$), figure 5. An isotopic shift of ~34 cm^{-1} is well below what would be expected for CO bound directly to the electrode surface, where values of ~100 cm^{-1} are typical, allowing us to rule out this assignment.[41] Instead we propose that the isotopic shift arises from either vibronic coupling between the Mn-$^{13}C^{18}O_2H$ and Mn-CO groups (feasible with **6,7**) or from the presence of Mn-$^{13}C^{18}O$ groups (i.e. **8**, **9**). DFT calculations of **6-9** using a Hg(100) 6x6 cell to approximately account for the role of the Au/Hg electrode surface have been carried out (computational details in the supplementary methods and supplementary figure 14, tables 2, 3). The computed vibrational wavenumbers are shown in figure 7 and listed in supplementary tables 4 to 22. Although **8** has not been previously observed *in-situ* during

catalysis, it has been synthesised[35] and characterised (ν(CO), 2118, 2044, 2023 and 1982 cm^{-1}) and the un-scaled computed values for **8** both in vacuo (2106, 2034, 2030, 2005 cm^{-1}) and at the model Hg surface (2100, 2026, 2021, 1997 cm^{-1}) are in good agreement with the experimental results in solvent phase. Complexes **6**-**9** all have vibrational modes to which the 1976 cm^{-1} feature could be assigned. However, upon isotopic substitution of either the Mn-CO_2H group (**6**,**7**) or a Mn-CO axial group (**8**,**9**) with $^{13}C^{18}O$, only the axially labelled complexes **8** (47-53 cm^{-1}) and **9** (41-52 cm^{-1}) show shifts comparable with the VSFG measured value of ~34 cm^{-1}. The lack of shift of the ν(CO) modes of **6** and **7** upon substitution of the Mn-CO_2H group excludes the possibility that these intermediates may be responsible for the VSFG spectra in the 1900-2000 cm^{-1} region.

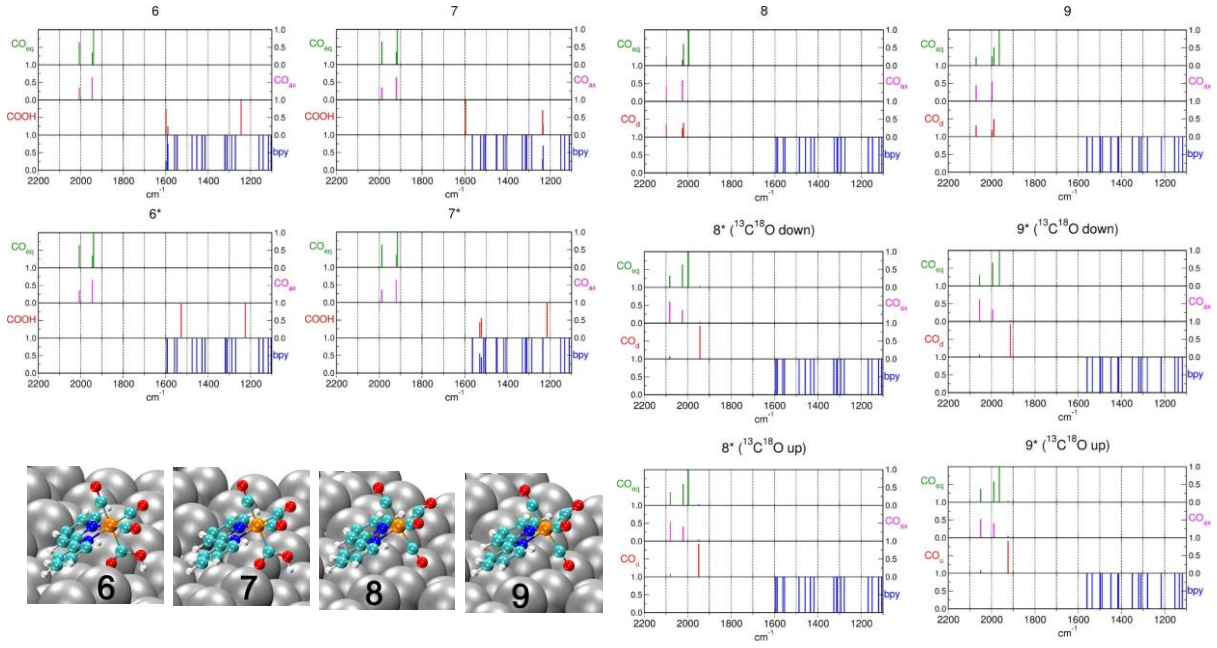

Figure 7: **Fragment-resolved analysis of the contributions to the computed IR modes (normalized eigenvectors) for 6-9**. *Analysis of the ν(CO) region allows for exclusion of assignment of the intermediate to **6** or **7** and the experimentally determined presence of a bpy mode at 1600 cm^{-1} (figure 5) is in alignment with assignment to **8**. Calculations carried out on the energetically favoured geometries of the pristine and isotopically labelled (*) complexes **6** to **9** on the model Hg(100)-6x6 surface. CO_{eq}: equatorial CO; CO_{ax}: axial CO; bpy: 2,2-bipyridine; CO_d: axial CO pointing towards the surface (down geometry), CO_u: axial CO pointing away from surface (up geometry). Hg(100): silver, H: white, C: cyan, O: red, N: blue, Mn: orange.*

Comparison between the calculated the highest-energy bpy modes of **8** (1594 cm^{-1}) and **9** (1559 cm^{-1}) and our observation of a VSFG band of the intermediate at 1600 cm^{-1} support assignment to complex **8** (figure 7, supplementary table 4). It is also significant that we observe Stark shifting of the intermediate ν(CO) band (*ca.* +17 cm^{-1} V^{-1}, -1.60 to -1.35 V) in figure 4. Calculations of the vibrational modes of **8** and **9** in the presence of an external electric-field also support assignment to **8**, figure 8. Only **8** has a CO mode that hardens upon reduction of the intensity of the external electric field. Although **8** was not predicted to accumulate, previous solution phase calculations indicated that **9** is thermally unstable and that the reduction potential of **9** (*ca* -1.1 V_{SCE}) is significantly positive of **8** (*ca* -1.3 V_{SCE}).[31,33] Caution should be taken when comparing to experimental data of molecules at an electrode surface to calculations in solution, nonetheless it interesting that here we find that the VSFG bands of the intermediate are stable for >50 s (supplementary figure 11) and that the intermediate builds in concentration and reaches a maximum between -1.1 and -1.2 V_{Ag} (*ca.* -1.3 to -1.4 V_{SCE}) figure 4b. We also only observe the new intermediate VSFG bands in the presence of stronger acids where the

protonation first pathway occurs (see below). Therefore on the balance of probability we assign the 1976 and 1600 cm^{-1} VSFG bands to CO stretching and bipyridine modes of **8**, an intermediate present during the protonation first pathway (**6**-**8**-**9**). To the best of our knowledge this represents the first experimental evidence of the protonation first pathway occurring with **1**.

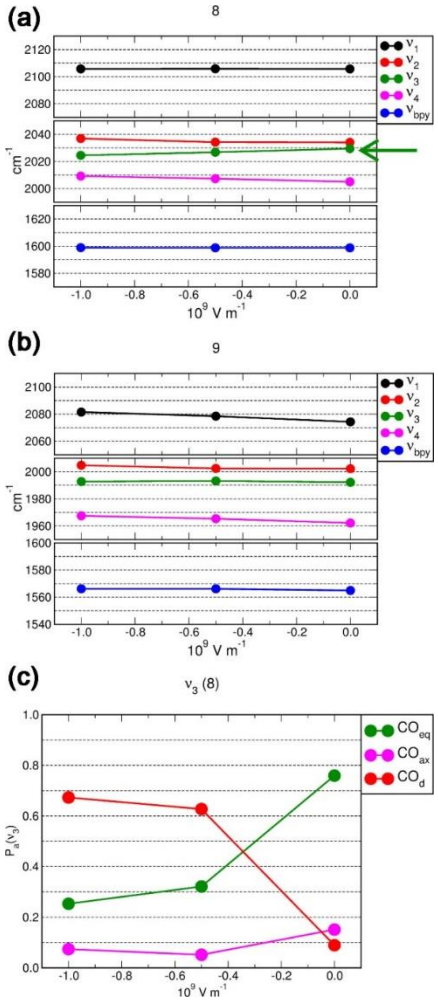

Figure 8: **Computed Stark shifts of the vibrational modes of 8 and 9** *Calculations of isolated complexes **8(a)** and **9(b)** show only one mode [ν_3(**8**)] is compatible with the measured Stark shift (field-induced vibrational softening) in figure 4. This is indicated with a green arrow. Molecules are oriented as per energy favoured adsorption geometry on the Hg surface and the external electrostatic field (V m^{-1}) is along the direction perpendicular to the pristine Hg-surface. For the sign convention used, more negative electric fields correspond to accumulation of more negative charge under the tripod formed by the Mn-bpy and Mn-CO_d bonds (see figure 7).* ***(c)*** *Computed dependence of the CO-contributions to ν_3(**8**) [$P_a(\nu_3)$]on the external electrostatic field: the contributions from CO_d (CO_{eq}) increase (decrease) with the intensity of the external electric field.*

The accumulation of **8** is unexpected, as although a Mn tetracarbonyl cation has recently been reported in catalysis studies of a N-heterocyclic carbene Mn complex,[42] microkinetic studies of **1** in solution predicted the accumulation of **6** when catalysis proceeds via the protonation first pathway.[32] However, DFT calculations of the protonation of **6** to **8** in solution also report that the equilibrium position can sit either towards **6** or **8** ($\Delta G_{6\text{-}8}$ range from +18 to -28 kcal mol^{-1}) depending on the model employed.[31–33] It is therefore apparent in real systems where the interaction of the complex with the electrode, solvent and surface electric field all need to be considered it is feasible that the interconversion of **6** to **8** may occur.

At potentials negative of -1.7 V_{SCE} (*ca.* -1.5 V_{Ag}) it is anticipated that the contribution from the protonation pathway to the catalytic current is minimal and that the reduction first pathway dominates and here we do not observe **8** at <-1.4 V_{Ag} (figure 4).[32,33] Following the loss of the VSFG modes assigned to **8** on the outward CV sweep we see the growth of a new broad, weak, VSFG mode at 1875 cm^{-1} which is transiently present at *ca.* -1.3 V_{Ag}, figure 6a. Although reasonable agreement exists with the calculated spectrum of **7**, an intermediate on the reduction first pathway, the VSFG band is weak and not detected in isotopic labelling experiments where a lower concentration of CO_2 is used, preventing assignment. Nonetheless, the loss of the VSFG spectral features of **8** at potentials where the reduction of **6** becomes viable provides strong evidence for the anticipated switch in pathway from protonation first to reduction first at more negative potentials.

We have also examined the role of Brønsted acid strength on the mechanism of CO_2 reduction using VSFG. Interestingly the catalytic current at -1.35 V_{Ag}, a potential where contribution from only the protonation first pathway is expected, correlates with the intensity of the ν(CO) mode of **8** and the acid pKa, figure 4(c). It has been calculated that the protonation first pathway requires stronger acids (TFE pKa(CH_3CN) = 26.4, phenol pKa(CH_3CN) = 21.6)) to enable both the initial protonation assisted binding of CO_2 (**3-5-6**) and the protonation of **6** to form **8**.[32,33] Indeed we see very similar VSFG spectra with phenol, with **8** clearly present between *ca.* -1.1 and -1.4 V_{Ag}, supplementary figure 12.[32] In contrast with methanol, a weaker acid (pKa(CH_3CN) = 30.5), we observe no evidence of **8** by VSFG and minimal catalytic current enhancement at -1.35 V_{Ag}, supplementary figures 6,13. It is calculated that the protonation first pathway is largely inactive using methanol in-line with this observation.[32]

Clearly to form **8** and access the protonation first pathway either a suitably strong acid in solution, or the use of ligands with pendant group to orientate and enable protonation by weaker acids, is required and promising results using such an approach have recently been reported.[21,28] The observed accumulation of **8** at the Au-Hg surface over a wide potential window indicates that developing analogues of **8** with more positive reduction potentials may be a route to higher TOF at lower overpotentials in systems where protonation first can occur. However this will need to be balanced with the need to generate sufficiently nucleophilic metal centres for CO_2 reduction to occur at. [43] The results presented above represent a significant step forward in understanding the remarkable properties of **1** for the reduction of CO_2 to CO and more widely demonstrate the importance of VSFG spectroscopy as a technique to deliver the design rules required for more efficient molecular electrocatalysts.

Conclusions

We report the mechanisms of the very widely studied CO_2 reduction electrocatalyst **1** in the presence of a range of different Brønsted acids. VSFG experiments allowed for the detection of a species not seen in analogous FTIR-SEC studies, assigned to $[Mn(bpy)(CO)_4]^+$ (**8**), an intermediate of the low overpotential protonation first mechanism. DFT calculations and VSFG experiments in weak (methanol) and stronger (TFE, phenol) acids and isotopic labelling support the assignment of **8**. Although our study supports the theory derived mechanisms, the accumulation of **8** is unexpected suggesting that protonation of a Mn-CO_2H intermediate (**6**) readily occurs using TFE and phenol at our electrode surface. Of significance is the demonstrated application of VSFG to the study of molecular electrocatalytic mechanisms. We are now exploring the applicability of the approach to a wider range of molecular electrocatalysts, electrodes and reactions with potential applications across energy storage and conversion.

Methods

Experimental methods. Bromopentacarbonylmanganese(I) (98%), 2,2'-bipyridine (99%), acetonitrile (anhydrous, 99.8%), 2,2,2-trifluoroethanol (TFE, ≥99.5%), methanol (MeOH, 99.8%), tetrabutylammonium trifluorophosphate ($TBAPF_6$, ≥99.0%), phenol (≥99.0%), and $^{13}C^{18}O_2$ (99 atom % ^{13}C, 95 atom % ^{18}O) were purchased from Sigma Aldrich and used as received. Ferrocene (Sigma, ≥98%) was further purified *via* sublimation, then dried under vacuum. $Mn(bpy)(CO)_3Br$ was synthesized as previously reported.[44]

Spectroelectrochemical (SEC) experiments were carried out using a custom-made cell described elsewhere.[16] The cell consists of a Teflon cross piece containing the working electrode, a Pt counter electrode an a Ag/Ag^+ *pseudo*-reference electrode. The addition of ferrocene (Fc) to the single compartment SEC cell during VSFG studies was not possible as the optical properties of Fc/Fc^+ (which changes in concentration during the experiment due to the proximity of the counter electrode) complicate data analysis. Therefore in the main text potentials are reported *versus* the Ag/Ag^+ *pseudo* reference electrode. *Ex-situ* experiments (supplementary figure 1) using the same working and reference electrodes in a standard three electrode cell indicate that Fc/Fc^+ ~ 0.60 V *versus* the silver *pseudo*-reference electrode, allowing us to estimate the reduction potentials of **1** and **2** to be -1.12 V and -1.47 V *versus* SCE. During SEC experiments the distance between the working electrode and the CaF_2 front window is *ca.* 50 μm, set by a Teflon spacer. The working electrode was a polycrystalline gold disc (Ø = 16 mm, IJCambria) that had been in immersed in mercury (polarographic grade, Fisher) for 1 minute before being left to dry in a fumehood for at least 2 hours. The Au-Hg electrode is then hand-polished (*suitable care should be taken to avoid exposure to small Au-Hg particles*) using decreasing sizes of polishing pastes (15 μm and 6 μm diamond paste, then 0.5 μm alumina slurry) for 5 minutes each (the electrode was sonicated in milli-Q water for 30 seconds between each polish), to yield a silver-yellow electrode which was reflective enough to allow for alignment and measurements. A palmsens3 potentiostat was used to carry out all the electrochemical experiments.

The SFG experiments were carried out in the Central Laser Facility at the STFC Rutherford Appleton Laboratory using the Ultra B laser system. The SFG apparatus has been reported elsewhere.[16] Typical pulse energies for the 800 nm beam were < 1 μJ (10 kHz) to ensure no laser heating or damage, while the fs IR pulse (500 cm^{-1} useable bandwidth) was set to pulse energies of 2-3 μJ. The beams were focussed at the electrode with spot sizes of ~200 and ~300 um. To suppress the non-resonant background in the SFG data, the SFG spectra were acquired using a short delay (typically 0.9 ps) between the fs IR pulse and the fs derived time asymmetric visible (800 nm) pulse as previously described.[36] All experiments were conducted with *ppp* polarisation and all analysis was based on identifying band frequencies, rather than assessing orientation changes from band intensity changes. For spectroelectrochemical experiments carried out at 10 mV s^{-1} SFG spectra were collected every one or four seconds and were a result of a one or four seconds averaging, respectively.

Computational methods: All the Density Functional Theory simulations were performed with the projector-augmented wave (PAW) method[45] as implemented in the VASP program,[46–48] the PBE approximation to the exchange-correlation (XC) functional,[49] 400 eV plane wave energy cut-off, 0.1 eV Gaussian smearing, and Grimme D2 van der Waals (vdW) corrections.[50] Following the original approach of identical parameterisation of vdW-corrections for *3d* (Sc-Zn) and an *4d* (Y-Cd) transition metals,[50]the parameters for Hg-atoms, not included in the original parameterisation,[50] were taken from reference[51](C_6 = 40.62 J nm^6 mol^{-1}, R_0 = 1.772 Å). Fully unconstrained spin-polarisation was used for those system containing an odd number of electrons (e.g. **7** and **9**), resulting in a total magnetic moment of 1 μ_B.

Following reference[52], the electrode surface was approximated by a one-layer rhombohedral Hg(100)-6x6 slab (36 Hg atoms), leading to an hexagonal simulation cell with 20.1936 Å optimised (in-plane) lattice vectors. Complexes were placed on one side of the slab ensuring at least 12 Å vacuum-buffer

was present between periodic replicas of the slab models (with adsorbates). The slab 2D Brillouin zone was sampled with a grid of 5 (Γ-centred) symmetry irreducible **k**-points.

For geometry optimisation, all the atoms of the Hg-slab and molecular adsorbates were fully relaxed until the atomic forces were lower than 0.02 eV $Å^{-1}$. Harmonic vibrational frequencies were calculated *via* symmetric finite displacements of ±0.01 Å, maintaining the Hg-atoms fixed. Isotopically labelled systems were simulated by changing the atomic mass as needed in setting up the mass-weighted Hessian matrix ahead of diagonalization.

Defined $\mathbf{Q}^{(j)}$ the (normalized) vector representing the j^{th} vibrational mode (of wavenumber $\hat{\nu}_j$) in a 3D Cartesian reference, the contribution $P_a^{(j)}$ to $\mathbf{Q}^{(j)}$ from the a^{th} molecular fragment (a = CO_{eq}, CO_{ax}, *bpy*, *Mn*, reacting *COOH/CO* group) shown in figure 7 was computed by summing the square of the (three Cartesian) displacements for the atoms in a:

$$P_a^{(j)} = \sum_{i \in a} \left[Q_i^{(j)} \right]^2$$

For the definition used, vibrational modes fully localized on the ath fragment result in $P_a^{(j)} = 1$ values. Conversely, $0 < P_a^{(j)} < 1$ values reveal partially delocalized modes i.e. coupling between vibrations of different molecular fragments (e.g. different CO ligands).

Acknowledgements

We are grateful to Charlotte Smith (UoL) for synthesis of **1**. This work was carried out at the Ultra facility of the UK Central Laser Facility during experiments 15130005, 16130016 and 16230052. AC and GN acknowledge support from EPSRC (EP/K006851/1, EP/P034497/1 and EP/N010531/). GT acknowledges support from EPSRC (EP/I004483/1, EP/K013610/1, and EP/P022189/1). This work made use of the ARCHER (via the UKCP Consortium, EPSRC UK EP/K013610/1 and EP/P022189/1) and UK Materials and Molecular Modelling Hub (EPSRC UK EP/P020194/1) High-Performance Computing facilities.

Data availability

Raw data all figures within the paper is freely available from the University of Liverpool Research Data Catalogue at http://dx.doi.org/10.17638/datacat.liverpool.ac.uk/533.

Author contributions:

GN, AC, PD and JW have carried out the experimental work. GT has carried out the computational work. AC and GT wrote the manuscript. All authors have contributed to the editing of the manuscript.

Competing interests:

The authors declare no competing interests

References

1. Dey, S. *et al.* Molecular electrocatalysts for the oxygen reduction reaction. *Nat. Rev. Chem.* **1,** 98 (2017).

2. DuBois, D. L. Development of Molecular Electrocatalysts for Energy Storage. *Inorg. Chem.* **53,** 3935–3960 (2014).

3. Costentin, C., Robert, M. & Savéant, J.-M. Catalysis of the electrochemical reduction of carbon dioxide. *Chem. Soc. Rev.* **42,** 2423–2436 (2013).

4. Lee, K. J., Elgrishi, N., Kandemir, B. & Dempsey, J. L. Electrochemical and spectroscopic methods for evaluating molecular electrocatalysts. *Nat. Rev. Chem.* **1,** 39 (2017).

5. Shen, Y. R. Surface properties probed by second-harmonic and sum-frequency generation. *Nature* **337,** 519–525 (1989).

6. Shen, Y. R. Basic Theory of Surface Sum-Frequency Generation. *J. Phys. Chem. C* **116,** 15505–15509 (2012).

7. Lambert, A. G., Davies, P. B. & Neivandt, D. J. Implementing the Theory of Sum Frequency Generation Vibrational Spectroscopy: A Tutorial Review. *Appl. Spectrosc. Rev.* **40,** 103–145 (2005).

8. Rey, N. G. & Dlott, D. D. Studies of electrochemical interfaces by broadband sum frequency generation. *J. Electroanal. Chem.* **800,** 114–125 (2017).

9. Baldelli, S. Probing Electric Fields at the Ionic Liquid−Electrode Interface Using Sum Frequency Generation Spectroscopy and Electrochemistry. *J. Phys. Chem. B* **109,** 13049–13051 (2005).

10. Liu, W.-T. & Shen, Y. R. In situ sum-frequency vibrational spectroscopy of electrochemical interfaces with surface plasmon resonance. *Proc. Natl. Acad. Sci.* **111,** 1293–1297 (2014).

11. Tadjeddine, A. *et al.* Sum and Difference Frequency Generation at the Electrochemical Interface. *Phys. status solidi* **175,** 89–107 (1999).

12. Anfuso, C. L. *et al.* Orientation of a Series of CO_2 Reduction Catalysts on Single Crystal TiO_2 Probed by Phase-Sensitive Vibrational Sum Frequency Generation Spectroscopy (PS-VSFG). *J. Phys. Chem. C* **116,** 24107–24114 (2012).

13. Ge, A. *et al.* Surface-Induced Anisotropic Binding of a Rhenium CO_2-Reduction Catalyst on Rutile TiO_2(110) Surfaces. *J. Phys. Chem. C* **120,** 20970–20977 (2016).

14. Anfuso, C. L., Ricks, A. M., Rodríguez-Córdoba, W. & Lian, T. Ultrafast Vibrational Relaxation Dynamics of a Rhenium Bipyridyl CO2 Reduction Catalyst at a Au Electrode Surface Probed by Time-Resolved Vibrational Sum Frequency Generation Spectroscopy. *J. Phys. Chem. C* **116,** 26377–26384 (2012).

15. Wang, J. *et al.* Short-Range Catalyst–Surface Interactions Revealed by Heterodyne Two-Dimensional Sum Frequency Generation Spectroscopy. *J. Phys. Chem. Lett.* **6,** 4204–4209 (2015).

16. Neri, G., Donaldson, P. M. & Cowan, A. J. The Role of Electrode–Catalyst Interactions in Enabling Efficient CO_2 Reduction with $Mo(bpy)(CO)_4$ As Revealed by Vibrational Sum-Frequency Generation Spectroscopy. *J. Am. Chem. Soc.* **139,** 13791–13797 (2017).

17. Tory, J., Setterfield-Price, B., Dryfe, R. A. W. & Hartl, F. [$M(CO)_4$ (2,2′-bipyridine)] (M=Cr, Mo, W) Complexes as Efficient Catalysts for Electrochemical Reduction of CO 2 at a Gold Electrode. *ChemElectroChem* **2,** 213–217 (2015).

18. Bourrez, M., Molton, F., Chardon-Noblat, S. & Deronzier, A. [Mn(bipyridyl)$(CO)_3$Br]: an abundant metal carbonyl complex as efficient electrocatalyst for CO2 reduction. *Angew. Chem. Int. Ed. Engl.* **50,** 9903–9906 (2011).

19. Stanbury, M., Compain, J.-D. & Chardon-Noblat, S. Electro and photoreduction of CO_2 driven by manganese-carbonyl molecular catalysts. *Coord. Chem. Rev.* **361,** 120–137 (2018).

20. Sampson, M. D. & Kubiak, C. P. Manganese Electrocatalysts with Bulky Bipyridine Ligands:

Utilizing Lewis Acids To Promote Carbon Dioxide Reduction at Low Overpotentials. *J. Am. Chem. Soc.* **138,** 1386–1393 (2016).

21. Ngo, K. T. *et al.* Turning on the Protonation-First Pathway for Electrocatalytic CO_2 Reduction by Manganese Bipyridyl Tricarbonyl Complexes. *J. Am. Chem. Soc.* **139,** 2604–2618 (2017).

22. Walsh, J. J., Neri, G., Smith, C. L. & Cowan, A. J. Electrocatalytic CO_2 reduction with a membrane supported manganese catalyst in aqueous solution. *Chem. Commun.* **50,** 12698–12701 (2014).

23. Walsh, J. J. *et al.* Improving the efficiency of electrochemical CO_2 reduction using immobilized manganese complexes. *Faraday Discuss.* **183,** 147–160 (2015).

24. Reuillard, B. *et al.* Tuning Product Selectivity for Aqueous CO_2 Reduction with a Mn(bipyridine)-pyrene Catalyst Immobilized on a Carbon Nanotube Electrode. *J. Am. Chem. Soc.* **139,** 14425–14435 (2017).

25. Hartl, F., Rossenaar, B. D., Stor, G. J. & Stufkens, D. J. Role of an electron-transfer chain reaction in the unusual photochemical formation of five-coordinated anions Mn(CO)(3)(alpha-diimine) (-) from fac- Mn(X)(CO)$_{(3)}$(alpha-diimine) (X=halide) at low temperatures. *Recl. Trav. Chim. Pays-Bas* **114,** 565- (1995).

26. Bourrez, M. *et al.* Pulsed-EPR evidence of a manganese(II) hydroxycarbonyl intermediate in the electrocatalytic reduction of carbon dioxide by a manganese bipyridyl derivative. *Angew. Chem. Int. Ed. Engl.* **53,** 240–243 (2014).

27. Rossenaar, B. D. *et al.* Electrochemical and IR/UV−Vis Spectroelectrochemical Studies of fac-[Mn(X)$(CO)_3$(iPr-DAB)]n (n = 0, X = Br, Me, Bz; n = +1, X = THF, MeCN, nPrCN, $P(OMe)_3$; iPr-DAB = 1,4-Diisopropyl-1,4-diaza-1,3-butadiene) at Variable Temperatures: Relation between Electr. *Organometallics* **16,** 4675–4685 (1997).

28. Franco, F. *et al.* Local Proton Source in Electrocatalytic CO_2 Reduction with [Mn(bpy-R)$(CO)_3$Br] Complexes. *Chem. - A Eur. J.* **23,** 4782–4793 (2017).

29. Hartl, F., Rosa, P., Ricard, L., Le Floch, P. & Záliš, S. Electronic transitions and bonding properties in a series of five-coordinate '16-electron' complexes $[Mn(CO)_3(L_2)]^-$ (L_2= chelating redox-active π-donor ligand). *Coordination Chemistry Reviews* **251,** 557–576 (2007).

30. Hawecker, J., Lehn, J.-M. & Ziessel, R. Electrocatalytic reduction of carbon dioxide mediated by Re(bipy)$(CO)_3$Cl (bipy = 2,2′-bipyridine). *J. Chem. Soc. Chem. Commun.* **0,** 328–330 (1984).

31. Riplinger, C., Sampson, M. D., Ritzmann, A. M., Kubiak, C. P. & Carter, E. A. Mechanistic Contrasts between Manganese and Rhenium Bipyridine Electrocatalysts for the Reduction of Carbon Dioxide. *J. Am. Chem. Soc.* **136,** 16285–16298 (2014).

32. Riplinger, C. & Carter, E. A. Influence of Weak Brønsted Acids on Electrocatalytic CO_2 Reduction by Manganese and Rhenium Bipyridine Catalysts. *ACS Catal.* **5,** 900–908 (2015).

33. Lam, Y. C., Nielsen, R. J., Gray, H. B. & Goddard, W. A. A Mn Bipyrimidine Catalyst Predicted To Reduce CO_2 at Lower Overpotential. *ACS Catal.* **5,** 2521–2528 (2015).

34. Grills, D. C. *et al.* Mechanism of the Formation of a Mn-Based CO_2 Reduction Catalyst Revealed by Pulse Radiolysis with Time-Resolved Infrared Detection. *J. Am. Chem. Soc.* **136,** 5563–5566 (2014).

35. Scheiring, T., Kaim, W. & Fiedler, J. Geometrical and electronic structures of the acetyl complex Re(bpy)$(CO)_3(COCH_3)$ and of [M(bpy)$(CO)_4$](OTf), M=Mn,Re. *J. Organomet. Chem.* **598,** 136–141 (2000).

36. Lagutchev, A., Lozano, A., Mukherjee, P., Hambir, S. A. & Dlott, D. D. Compact broadband

vibrational sum-frequency generation spectrometer with nonresonant suppression. *Spectrochim. Acta Part A Mol. Biomol. Spectrosc.* **75,** 1289–1296 (2010).

37. Bishop, D. M. The vibrational Stark effect. *J. Chem. Phys.* **98,** 3179–3184 (1993).

38. Ohno, P. E., Wang, H. & Geiger, F. M. Second-order spectral lineshapes from charged interfaces. *Nat. Commun.* **8,** 1032 (2017).

39. Keith, J. A., Grice, K. A., Kubiak, C. P. & Carter, E. A. Elucidation of the Selectivity of Proton-Dependent Electrocatalytic CO_2 Reduction by fac-Re(bpy)(CO)$_3$Cl. *J. Am. Chem. Soc.* **135,** 15823–15829 (2013).

40. Sampson, M. D. *et al.* Manganese catalysts with bulky bipyridine ligands for the electrocatalytic reduction of carbon dioxide: eliminating dimerization and altering catalysis. *J. Am. Chem. Soc.* **136,** 5460–5471 (2014).

41. Borovkov, V. Y., Kolesnikov, S. P., Kovalchuk, V. I. & D'Itri, J. L. Probing Adsorption Sites of Silica-Supported Platinum with $^{13}C^{16}O$ + $^{12}C^{16}O$ and $^{13}C^{18}O$ + $^{12}C^{16}O$ Mixtures: A Comparative Fourier Transform Infrared Investigation. *J. Phys. Chem. B* **109,** 19772–19778 (2005).

42. Lloret-Fillol, J., Franco, F., Pinto, M. F. & Royo, B. A Highly Active N-heterocyclic Carbene MnI complex for Selective Electrocatalytic CO_2 Reduction to CO. *Angew. Chemie Int. Ed.* **10,** (2018).

43. Smieja, J. M. & Kubiak, C. P. Re(bipy-tBu)(CO)$_3$ Cl−improved Catalytic Activity for Reduction of Carbon Dioxide: IR-Spectroelectrochemical and Mechanistic Studies. *Inorg. Chem.* **49,** 9283–9289 (2010).

44. Walsh, J. J., Neri, G., Smith, C. L. & Cowan, A. J. Electrocatalytic CO 2 reduction with a membrane supported manganese catalyst in aqueous solution. *Chem. Commun.* **50,** 12698–12701 (2014).

45. Blöchl, P. E. Projector augmented-wave method. *Phys. Rev. B* **50,** 17953–17979 (1994).

46. Kresse, G. & Furthmüller, J. Efficiency of *ab-initio* total energy calculations for metals and semiconductors using a plane-wave basis set. *Comput. Mater. Sci.* **6,** 15–50 (1996).

47. Kresse, G. & Furthmüller, J. Efficient iterative schemes for ab initio total-energy calculations using a plane-wave basis set. *Phys. Rev. B - Condens. Matter Mater. Phys.* **54,** 11169–11186 (1996).

48. Joubert, D. From ultrasoft pseudopotentials to the projector augmented-wave method. *Phys. Rev. B - Condens. Matter Mater. Phys.* **59,** 1758–1775 (1999).

49. Perdew, J., Burke, K. & Ernzerhof, M. Generalized Gradient Approximation Made Simple. *Phys. Rev. Lett.* **77,** 3865–3868 (1996).

50. Grimme, S. Semiempirical GGA-type density functional constructed with a long-range dispersion correction. *J. Comput. Chem.* **27,** 1787–1799 (2006).

51. Amft, M., Lebègue, S., Eriksson, O. & Skorodumova, N. V. Adsorption of Cu, Ag, and Au atoms on graphene including van der Waals interactions. *J. Phys. Condens. Matter* **23,** 395001 (2011).

52. Wu, Y. *et al.* Electrode-Ligand Interactions Dramatically Enhance CO_2 Conversion to CO by the [Ni(cyclam)](PF_6)$_2$Catalyst. *ACS Catal.* **7,** 5282–5288 (2017).